Biochemistry **2002,** *41,* 10472−10481

Structural Mobility of the Extracellular Ligand-Binding Core of an Ionotropic Glutamate Receptor. Analysis of NMR Relaxation Dynamics[†]

Robert L. McFeeters and Robert E. Oswald*

Department of Molecular Medicine, Cornell University, Ithaca, New York 14853

Received April 23, 2002; Revised Manuscript Received June 18, 2002

ABSTRACT: Ionotropic glutamate receptors play important roles in a variety of neuronal processes and have been implicated in multiple neurodegenerative diseases. The extracellular ligand-binding (S1S2) core of the GluR2 subtype can be expressed in bacteria as a soluble, monomeric protein with binding properties essentially identical to those of the intact receptor. The crystal structure of this protein has been determined in the presence and absence of various agonists and antagonists [Armstrong, N., Sun, Y., Chen, G. Q., and Gouaux, E. (1998) *Nature 395*, 913−917; Armstrong, N., and Gouaux, E. (2000) *Neuron 28*, 165−181]. The protein consists of two lobes, with the S1 segment composing the majority of lobe 1 and the S2 segment composing most of lobe 2. A domain closure upon ligand binding has been postulated, but details of intradomain motions have not been investigated. In this paper, the backbone motions of the ligand-binding core of GluR2 bound to glutamate were studied using ^{15}N longitudinal (T_1) and transverse (T_2) relaxation measurements as well as $\{^1\text{H}\}-^{15}\text{N}$ nuclear Overhauser effects at 500 and 600 MHz. Residues in the agonist-binding pocket exhibited two main classes of motion. Those contacting the α-substituents of the ligand glutamate exhibited minimal internal motion, while those contacting the γ-constituents exhibited exchange dynamics, indicating two dynamically distinct portions of the binding pocket. Also, two residues in transdomain linkers between lobes 1 and 2 show exchange, lending new insight into the previously proposed domain closure hypothesis. Finally, concerted motion of helix F suggests a pathway for ligand dissociation without the necessity of domain reopening.

Ionotropic glutamate receptors (iGluRs)[1] are found predominantly in the central nervous system of higher vertebrates where they mediate a majority of excitatory synaptic transmission (*1*). iGluRs also play important roles in neuronal development as well as in the formation of synaptic plasticity underlying higher-order processes such as learning and memory (*2*, *3*). They have been implicated in various neurologic disorders, including epilepsy, ischemic brain damage, and neurodegenerative disorders such as Parkinson's and Alzheimer's diseases and Huntington's chorea. More recently, iGluRs have been found to be involved in functions outside the central nervous system as well. Examples include iGluR expression in pancreatic islet cells modulating insulin secretion (*4*, *5*), iGluRs in osteoclasts and osteoblasts that modulate bone resorption (*6*, *7*), evidence for the presence of iGluRs in small, unmyelinated sensory nerve terminals in the skin (*8*, *9*), and expression of numerous iGluRs in the cardiac ganglia (*10*). With such findings, the therapeutic potential of drugs targeted to iGluRs is rapidly expanding, fueling the need for a better understanding of iGluRs on a molecular level.

In recent years, many advances in characterizing the relationship between iGluR structure and function have been made. iGluRs are membrane-bound receptor ion channels composed of multiple subunits arranged as a rosette, forming a central ion channel in which each subunit contributes to pore formation (*1*). Individual subunits are categorized by pharmacological properties, sequence, functionality, and biological role into those that are sensitive (1) to the synthetic agonist NMDA and requiring glycine as a co-agonist (NMDAR1,2A-D), (2) to the synthetic agonist AMPA (GluR1-4), or (3) to the naturally occurring neurotoxin kainate (GluR5-7, KA1,2).

Originally, the transmembrane topology of iGluRs was thought to be similar to that of other ligand-gated ion channels (such as the nicotinic acetylcholine receptor), having four transmembrane segments and a large cytoplasmic loop. Sequence analysis, however, revealed a homology between iGluRs and certain amino acid binding proteins (*11*, *12*), which included both a portion of the extracellular N-terminal

---

[†] This work was supported by Grant IBN 9974604 from the National Science Foundation. R.L.M. thanks the PHrMA Foundation for financial support.

* To whom correspondence should be addressed: Department of Molecular Medicine, College of Veterinary Medicine, Cornell University, Ithaca, NY 14853. Phone: (607) 253-3877. Fax: (607) 253-3659. E-mail: reo1@cornell.edu.

[1] Abbreviations: AMPA, α-amino-3-hydroxy-5-methyl-4-isoxazolepropionic acid; D_t, coefficient of self-diffusion; iGluR, ionotropic glutamate receptor; IPTG, isopropyl β-D-thiogalactopyranoside; NMDA, *N*-methyl-D-aspartic acid; NMR, nuclear magnetic resonance; NOE, nuclear Overhauser effect; PEP, preservation of equivalent pathways; R_{ex}, chemical exchange rate; R_h, hydrodynamics radius; S1S2, ligand-binding core of GluR2; S^2, generalized order parameter; ST2, single transition to single transition; T_1 ($1/R_1$), longitudinal relaxation time; T_2 ($1/R_2$), transverse relaxation time; τ_e, effective correlation time for internal motions; τ_m, molecular or global correlation time; TROSY, transverse relaxation optimized spectroscopy. S1 refers to a peptide sequence N-terminal to M1, and S2 refers to the extracellular peptide sequence between M3 and M4. The terms lobe 1 and lobe 2 refer to the structural elements that make up the ligand-binding core.

10.1021/bi026010p CCC: $22.00

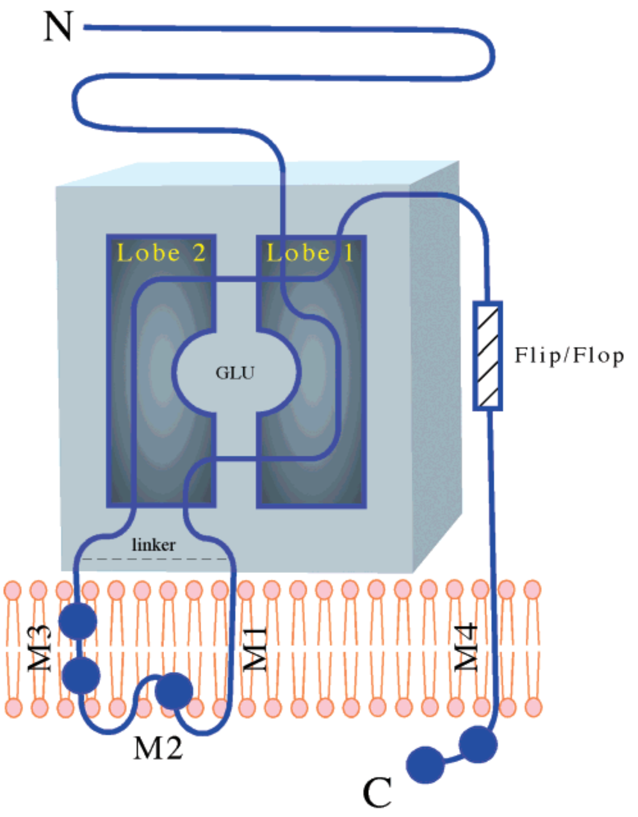

FIGURE 1: Graphical illustration of iGluR subunit topology. The gray box delineates the extracellular ligand-binding core S1S2. The agonist (GLU), individual lobes (lobe 1 and lobe 2), artificial linker (dashed line), flip-flop (hatched box), and transmembrane segments (M1−M4) are labeled. Circles represent typical sites of post-transcriptional/post-translation modification.

domain and the presumed large cytoplasmic loop. Using a variety of techniques, including mapping of glycosylation sites, deletion of presumed transmembrane segments, epitope mapping, and engineering of protease sites, kainate (*13*), AMPA (*14*), and NMDA glutamate receptors (*15*) were shown to have three transmembrane segments (M1, M3, and M4 as illustrated in Figure 1) with a reentrant loop (M2) comprising a portion of the ion channel. With the introduction of this topology, the regions of iGluRs homologous to bacterial amino acid binding proteins were shown to be extracellular. In particular, the N-terminal portion of the protein is homologous to a leucine-isoleucine-valine binding protein. The remainder of the N-terminal segment directly preceding M1 (S1) and the region between M3 and M4 (S2) comprise the ligand-binding core which is homologous to the lysine-arginine-ornithine binding protein and the glutamine binding protein. In addition, the sequence comprising the channel region was shown to be homologous to a portion of a potassium channel, though rotated 180° relative to the membrane (*16*, *17*). Thus, glutamate receptors are modular proteins made up of domains, for the most part, which are homologous with bacterial proteins (*16*). The C-terminal domain is highly variable and not structurally related to any specific bacterial protein; however, it can serve as a regulatory domain as well as a point of contact with intracellular proteins (*16*). Interestingly, a bacterial iGluR (GluR0) has been identified (*18*) that is truncated before M4 and has been proposed to be a missing evolutionary link between potassium and glutamate receptor channels.

Excision of the ligand-binding core from several iGluR subunits has resulted in soluble proteins having pharmacological properties very similar to those of intact membrane-bound receptors (*19*−*21*). A high-resolution crystal structure of the ligand-binding core of GluR2 bound to kainate was first reported in ref *22*. Soon after, structures of the GluR2 and GluR0 extracellular binding cores bound to other ligands as well as the unbound apo state were described (*23*, *24*). From these structures, evidence supporting a relationship between domain closure and activation was proposed, with the idea being that domain closure is related to channel activation. Though the crystal structures provided considerable insight into iGluR agonist−receptor interactions, they are largely static representations of a dynamic system. Using NMR relaxation measurements of the N−H backbone bond vector, we present here the dynamic properties of the ligand-binding core of GluR2 bound to glutamate, which provides evidence supporting a mechanism of domain closure and reveals unexpected disorder in parts of the agonist-binding pocket as well as in lobe 2.

EXPERIMENTAL PROCEDURES

Protein Expression and Purification. A perdeuterated ^{15}N sample was prepared by growing BL-21* *Escherichia coli* containing the S1S2 protein in a kanamycin resistant pET vector (Invitrogen, Carlsbad, CA) kindly provided by E. Gouaux (Columbia University, New York, NY) in 100% D_2O M9 medium. Extra care was taken to exchange all protons for deuterons in every component of the medium. Bacteria transformed with the S1S2 plasmid were conditioned to grow in fully deuterated medium by increasing the D_2O percentage in four equal steps. Once the bacteria were adapted, deuterated acetate was substituted for glucose as the sole carbon source. A 50 mL culture grown to saturation was used to seed a 1.25 L culture of fully exchanged M9 medium containing 2.5 g/L ammonium chloride and 4 g/L acetate. The culture was grown at 37 °C to an OD_{560} of approximately 0.8. Protein expression was induced with 0.5 mM IPTG (isopropyl β-D-thiogalactopyranoside) for 20 h before harvesting bacteria and freezing the cell pellets for later use.

S1S2 was purified and refolded, and NMR samples were prepared as described previously (*22*, *25*). Glutamate was present at 10 mM for all NMR samples. All data were obtained from a 250 μL sample of 600 μM fully deuterated [^{15}N]S1S2 in 5% D_2O. The level of deuterium substitution at nonlabile sites was estimated to be greater than 95% by comparison of amide to aliphatic peak heights obtained from one-dimensional ^{1}H spectra from fully deuterated and fully protonated samples in identical buffer. Complete exchange of amide deuterons for protons is expected due to the extent of exposure to protons in solvent during the denatured purification.

NMR Spectroscopy. NMR experiments were performed on Varian Inova spectrometers equipped with triple-resonance, *z*-gradient probes operating at 11.7 T (500 MHz for ^{1}H) and 14.1 T (600 MHz for ^{1}H) corresponding to 50.64 and 60.79 MHz ^{15}N frequencies, respectively. All relaxation measurements were performed at 25 °C with the probe temperature calibrated using a methanol standard (Cambridge Isotope Labs) as previously described (*26*, *27*). The carrier frequency for the directly detected ^{1}H dimension was set to the water resonance, and the spectral widths were 6.4 and 8.3 ppm for 500 and 600 MHz, respectively. The ^{15}N carrier frequency was set to 116.0 ppm, and the spectral width was set to 39.5 ppm for both fields. Previously reported ^{1}H and ^{15}N assignments (BMRB accession number 5182) were used (*25*). TROSY-based pulse sequences implementing ST2 polarization transfer instead of a PEP sequence were used for all data collection (*28*).

Longitudinal ^{15}N relaxation, transverse ^{15}N relaxation, and heteronuclear NOEs were measured at both 500 and 600 MHz. At 600 MHz, T_1 relaxation experiments employed longitudinal delay times of 12 (3), 164 (2), 326 (3), 489 (3), 651 (2), 1085 (2), 2168 (2), and 2710 (2) ms, where the number in parentheses indicates the number of spectra collected. T_2 experiments employed CPMG delays of 19 (3), 38 (3), 57 (3), 76 (2), 94 (2), and 132 (1) ms. Delay times for experiments at 500 MHz were almost identical, though slightly reduced due to shortened RF pulse lengths. Recycle delays were set to 1.6 s, and 16 scans per increment were collected for all T_1 and T_2 experiments. The heteronuclear NOE was recorded with and without broadband ^{1}H saturation for both field strengths using a saturation time of 6 s and recycle delay of 12 s. Thirty-two and 48 scans per increment were collected at 600 and 500 MHz, respectively, for all NOE experiments. All spectra at both fields were collected with 1024 complex ^{1}H points and 192 complex ^{15}N points except for the 500 MHz NOE experiments in which only 96 complex ^{15}N points were collected.

NMR Data Processing and Analysis. All data sets were processed in a similar fashion using NMRPipe, visualized, and peak picked using PIPP, and volumes were calculated using nonlinear least-squares fitting implemented by nlinLS (*29*). The final size of all real data matrices was 2048 × 2048 points, resulting in a digital resolution of 2.44 Hz/point for ^{1}H and 1.17 Hz/point for ^{15}N for all experiments at 600 MHz and 1.56 Hz/point for ^{1}H and 0.98 Hz/point for ^{15}N for all experiments at 500 MHz. Sample degradation over the course of relaxation data acquisition was characterized and corrected for by comparing peak intensities from identical experiments recorded throughout the course of data collection. Optimal T_1 and T_2 exponential fits were determined by conjugate gradient minimization with zero intercept and errors generated by Monte Carlo simulation (*30*). Heteronuclear NOE values and standard deviations were obtained from all permutations of the ratio of peak volumes from repeated measurements of ^{1}H-saturated and unsaturated spectra.

Translational Diffusion. The coefficient of self-diffusion (D_t) for S1S2 was measured using a longitudinal encode–decode pulse sequence (*31*) and a sample of approximately 300 μM natural abundance protein in buffer, lyophilized and resuspended in D$_2$O. Due to overlapping ^{1}H signals from buffer components, area integrations of the aliphatic region could not be used. Instead, peak intensities for well-resolved groups of proton resonances were plotted against the square of the gradient strength. Lysozyme was used as a standard control for slope calibration. D_t for 2 mM lysozyme in a ^{1}H$_2$O/^{2}H$_2$O mixture at 298 K was taken to be 1.08×10^{-6} cm^2 s^{-1} (*31*). Data from experiments utilizing 10 different gradient strengths, ranging from 4 to 60 G, were analyzed. Increments of $^1/_8$, $^1/_4$, $^1/_2$, and $^3/_4$ maximum were run in triplicate to provide estimates of error in the exponential fit. Peak intensities were fit to the following equation:

$$\ln(I) = \ln(I_0) + G^2\gamma^2\delta^2(\Delta/3 - \delta/3)D_t \tag{1}$$

where I is the measured peak intensity, G is the gradient strength in Gauss per centimeter, γ is the gyromagnetic ratio of protons (26 753 rad s^{-1} G^{-1}), δ is the length of the gradient pulse (1.5 ms), Δ is the diffusion time between gradients (600 ms), and D_t is the self-diffusion rate. D_t was determined for a newly prepared sample of S1S2 and after 4 weeks at room temperature to verify the monomeric state of the protein over the entire duration of the ^{15}N relaxation measurements.

Global Tumbling. An initial estimate of the global correlation time was determined from a trimmed mean T_1/T_2 ratio (*32*) using the program tmest (A. G. Palmer, Columbia University). To get a better understanding of the importance of anisotropic diffusion, the point-mass inertia tensor for S1S2 was calculated from the crystal structure coordinates (*23*) using PDBINERTIA version 1.1 (A. G. Palmer, Columbia University). Since nonisotropic diffusion was potentially present, a second two-step procedure was used to estimate the global correlation time by retaining residues that held information about anisotropic tumbling (*33*). In short, a primary filter was applied to remove residues with an NOE of <0.65 and residues with low T_2 values not having corresponding high T_1 values indicative of anisotropic tumbling. From the residues that survived, an approximation of the global tumbling was determined by minimizing the error-weighted difference between the experimental and calculated T_1/T_2 ratios from the following equation (*34*):

$$\chi_g^{\ 2} = \sum_{i=1}^{N} \frac{\left[\left(\frac{T_{1i}}{T_{2i}}\right)_{\text{exp}} - \left(\frac{T_{1i}}{T_{2i}}\right)_{\text{calc}}\right]^2}{\sigma_i^{\ 2}} \tag{2}$$

in which $\chi_g^{\ 2}$ is the error-weighted difference, N is the total number of residues with complete relaxation data sets surviving the primary filter, $(T_{1i}/T_{2i})_{\text{exp}}$ and $(T_{1i}/T_{2i})_{\text{calc}}$ are the experimentally measured and calculated ratios of longitudinal and transverse relaxation for residue i, respectively, and $\sigma_i^{\ 2}$ is the measured error in T_{1i}/T_{2i}. Theoretical T_1/T_2 ratios were calculated from standard equations (*35*) using an anisotropic global tumbling spectral density function (*36*) and the previously calculated diffusion tensor. This initial estimate of the global tumbling time was then used to evaluate the quality of the fit to the Lipari–Szabo model of internal motions for all residues (*37*). As a second filter, residues that did not fit the Lipari–Szabo model were removed as were residues having a τ_f of >600 ps since they were likely to violate the fast internal motion assumption (i.e., that the term containing the correlation time describing the faster internal motion contributes a negligible amount to relaxation). Residues that survived both filters were then used to calculate optimal global tumbling parameters. Three models of global tumbling were evaluated, isotropic, axially symmetric anisotropic, and fully anisotropic, with the final choice being based on an F test (*38*). Initially, global tumbling parameters were characterized separately for each field, though an average value was used in the final motional characterization (*39*).

Table 1: Models Used in the Analysis of Backbone Dynamics

model	parameters	assumptions[a]
1	S^2	$S_s^2 = 1$, $\tau_f \rightarrow 0$, $\tau_s \rightarrow 0$, $R_{ex} = 0$
2	S^2 and τ_e	$S_s^2 = 1$, $\tau_e < \tau_m$, $R_{ex} = 0$
3	S^2 and R_{ex}	$S_s^2 = 1$, $\tau_f \rightarrow 0$, $\tau_s \rightarrow 0$
4	S^2, τ_e, and R_{ex}	$S_s^2 = 1$, $\tau_e < \tau_m$
5	S_s^2, S_f^2, and τ_e	$\tau_f \rightarrow 0$, $\tau_e < \tau_m$, $R_{ex} = 0$

[a] τ_f is assumed to be sufficiently fast that it makes a negligible contribution to the relaxation parameters in models 1, 3, and 5. For models 2 and 4, the slow component is absent and $\tau_f = \tau_e$. $S^2 = S_f^2$ in models 1−4. Models 3 and 4 are derived from models 1 and 2, respectively, by including a chemical exchange term, R_{ex}, in the relaxation model to accommodate chemical exchange and other pseudo-first-order processes that contribute to the decay of the transverse magnetization on time scales slower than the overall correlation time, τ_m.

Model-Free Analysis of Internal Motions. The relaxation properties of an amide ^{15}N nucleus in a diamagnetic protein are generally dominated by dipolar interactions with the directly bonded amide proton and contributions due to chemical shift anisotropy. With this assumption, the measured relaxation parameters R_1, R_2, and NOE can be expressed as linear combinations of the spectral density function in a set of well-known equations described elsewhere (*35*, *40*). The spectral density function can in turn be related to the generalized motional parameters: the generalized order parameter S^2, the overall rotational correlation time τ_m, the effective correlation time τ_e, and a chemical exchange term R_{ex}. For all model-free calculations, the constant for chemical shift anisotropy was taken to be −160 ppm (*41*, *42*) and 1.02 Å used for the internuclear N−H bond length.

A complete model-free analysis of internal motion and overall rotational diffusion was performed using the NORMAdyn software package (*33*) implementing a spectral density function for anisotropic rotational diffusion (*38*, *42*). Data were fit to the five standard models (Table 1) with the following adjustable parameters: S^2 (model 1), S^2 and τ_e (model 2), S^2 and R_{ex} (model 3), S^2, τ_e, and R_{ex} (model 4), and S_f^2, S_s^2, and τ_e (model 5). Model selection was performed as previously reported (*33*) based on a χ^2 comparison of calculated and experimental relaxation parameters (eq 3).

$$\chi^2 = \frac{(T_1^{\mathrm{exp}} - T_1^{\mathrm{calc}})^2}{\sigma_{T_1}{}^2} + \frac{(T_2^{\mathrm{exp}} - T_2^{\mathrm{calc}})^2}{\sigma_{T_2}{}^2} + \frac{(\mathrm{NOE}^{\mathrm{exp}} - \mathrm{NOE}^{\mathrm{calc}})^2}{\sigma_{\mathrm{NOE}}{}^2} \quad (3)$$

Where applicable, estimates of the time scale of chemical exchange were obtained from the differences in exchange at different field strengths in the form of a dimensionless parameter α (*43*). If α < 1, exchange is slow compared to the chemical shift time scale. If α > 1 but less than the theoretical limit of 2, exchange is fast in comparison to the chemical shift time scale. Due to substantial error in R_{ex}, values of α outside the expected range of 0−2 were observed. However, if α was greater than 1, chemical exchange was still assumed to be in fast exchange based on previous arguments (*43*, *44*).

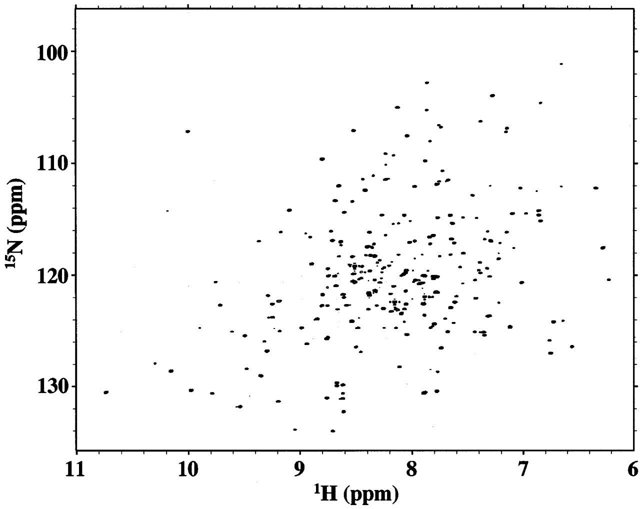

FIGURE 2: Results of a representative relaxation experiment for fully deuterated [^{15}N]S1S2. Protons are exchanged back onto the amide protons during purification in H_2O-containing solutions. The results of a T_1 experiment showing the correlation between amide proton and amide nitrogen resonances with a longitudinal delay time of 12 ms are shown.

Initially, characterization of global tumbling at both 500 and 600 MHz was treated separately. An average of the independently determined global tumbling parameters was then used to evaluate model selection and motional characterization for both fields since average global tumbling parameters are likely to be a more accurate representation of the actual molecular diffusion (*39*). Of the residues for which model selection was not identical at both fields, 90% differed by addition of a single parameter. Evaluation of the residual error in model selection and error in the original relaxation parameters were used as the basis for model determination. Preference was given to higher-field data, due to better resolution and an increased signal-to-noise ratio, and a simpler model. For the few cases in which model selection did not involve simple addition of one parameter, all were discrepancies in distinguishing between fast motion (model 2) and exchange (model 3). For these few cases, final model selection included considering motion of neighboring residues.

RESULTS AND DISCUSSION

NMR Data

Diffusional Translation. To ensure the protein remained monomeric throughout data acquisition, the self-diffusion rate (D_t) of S1S2 was measured using a pulsed field gradient method (*31*). Plots of ln(I) versus G^2 were linear over the range of gradient strengths used for experiments (eq 1) both with a freshly made sample and after the sample had been stored for 4 weeks at room temperature. The average self-diffusion rate for S1S2 was 1.43 ± 0.17 $cm^2\ s^{-1}$ and, within the uncertainties of the experiment, was independent of sample age and concentration, verifying the monomeric state of S1S2 throughout the entire duration of relaxation measurements.

Relaxation Data. To assess the backbone dynamics of S1S2, T_1, T_2, and NOE values at both 500 and 600 MHz were determined and data from both field strengths analyzed independently. Figure 2 shows the results of a representative T_1 experiment with a longitudinal delay time of 12 ms. Relaxation data for 241 residues, or 92% of the S1S2

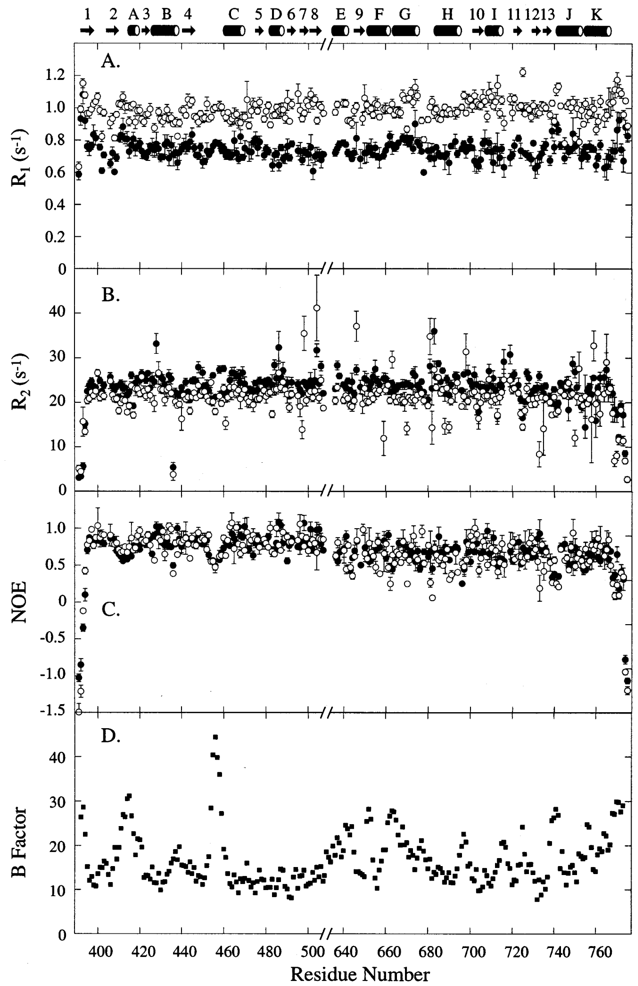

FIGURE 3: Relaxation parameters and associated errors for S1S2 shown as a function of residue number. The secondary structure is denoted above the plots: (A) longitudinal relaxation rate R_1, (B) transverse relaxation rate R_2, (C) heteronuclear NOE, and (D) nitrogen *B*-factor vs residue number (*22*). In panels A−C, the data taken at 500 MHz are shown as empty circles and those taken at 600 MHz are shown as filled circles. The numbering system used is that for the intact subunit. The break in the axis denotes the position of the artificial linker.

molecule, are presented. Residues 404, 457, 478, and 494, the last two residues of the artificial linkers, and residues 634, 635, 639, 679, 717, 718, and 737 are either unassigned or prolines (*25*). Also not present in the analysis are residues 390, 405, and 493, the third residue of the artificial linker, and residues 647, 658, 692, 695, 722, 744, and 763 due to incomplete relaxation data caused by resonance overlap or poor fitting. Figure 3A−C shows plots of all the relaxation parameters versus associated residue. The average values of R_1, R_2, and NOE at 600 (500) MHz excluding the disordered termini are 0.74 (0.98) ± 0.04 (0.03) s^{-1}, 23.98 (21.34) ± 1.12 (1.40) s^{-1}, and 0.82 (0.78) ± 0.06 (0.07), respectively. From theory, expected values (in the absence of chemical exchange) of R_1^{500}/R_1^{600}, R_2^{500}/R_2^{600}, and NOE^{500}/NOE^{600} are 1.32, 0.93, and 0.98, respectively (*40*). Measured average ratios agree well, having values of 1.33 ± 0.08, 0.92 ± 0.09, and 0.99 ± 0.13, respectively. The average R_2/R_1 ratio at 500 MHz (21.33 ± 1.62) is considerably smaller than that at 600 MHz (31.74 ± 2.27). A correlation between NOE and nitrogen *B*-factor (*22*) is striking with residues having lower NOE values having heightened *B*-factors (Figure 3C,D). Such a direct correlation is not necessarily observed for all proteins (*45*, *46*).

Global Tumbling. From the trimmed mean square average R_2/R_1 ratios, the program tmest (A. Palmer, Columbia University) yielded similar τ_m values of 17.7 ± 0.7 ns at 500 MHz and 17.9 ± 0.6 ns at 600 MHz. However, these estimates do not account for anisotropic tumbling. Calculation of the point-mass inertia tensor from the crystal structure coordinates excluding the first and last two residues showed that S1S2 had principal moments with the ratio of 1.85:1.59: 1.00, suggesting non-negligible anisotropic diffusion. Thus, models of isotropic, axially symmetric, and fully anisotropic global tumbling were compared. After minimization of χ_g^2 for each model, the appropriate model was selected on the basis of an *F* test (*38*) to determine significant differences in χ_g^2. For both fields, axially symmetric and fully anisotropic diffusion had significantly reduced errors compared to simple isotropic tumbling. The increased complexity of fully anisotropic diffusion was not statistically justified over axially symmetric diffusion, having a more than 93% chance that the fit was improved by chance. Parameters characterizing axially symmetric global tumbling were estimated from two independent programs. Calculating the shape factor from residues that survived the two-step filter using NORMAdyn yielded a value of 1.18 ± 0.17 for 600 MHz and 1.15 ± 0.14 for 500 MHz (*33*). Virtually identical values were calculated using the program R2R1 version 1.11 (A. G. Palmer, Columbia University). Since both fields were treated separately, average tumbling parameters were used for calculation of internal motions (*39*). An estimate of the global correlation time was calculated from the equation $\tau_m = (6D_{iso})^{-1}$ where $D_{iso} = (2D_\perp + D_\|)/3$, yielding a τ_m value of 17.7 ± 0.2 ns.

Relaxation Parameters. At 600 MHz, T_1, T_2, and NOE relaxation parameters for 235 residues were determined. Using the average axially symmetric global tumbling parameters, only 12 residues were not fit by any dynamics model. At 500 MHz, relaxation parameters for 229 residues were determined with only four residues not fit to any model. The N-terminal glycine was not fit to any model due to the NH_2 terminus, though model 5 is predicted due to a relatively large negative NOE. In most cases for which the model selection differed between fields, model discrepancy involved addition of a single parameter (*39*, *47*). In total for both fields, of the 241 residues for which relaxation data were obtained, models for 235 were reliably determined.

NORMAdyn (*33*) was used to calculate tumbling parameters and characterize internal motions for individual residues. Plots of S^2, τ_e, and R_{ex} versus residue number are shown in Figure 4. A noticeable decrease in S^2 was observed for residues near the N- and C-termini, while extended internal regions exhibit exchange and internal motion. Independently characterizing backbone dynamics at two field strengths allowed two measurements of the dynamics parameters to be calculated, reducing artifacts. Where applicable, average values of dynamics parameters are reported. Figure 5A shows the S1S2 crystal structure with residues colored according to motional model. Not unexpectedly, the termini (which are absent from the crystal structure) are very mobile with an average S^2 of 0.44 compared to a value of 0.91 for the rest of the protein. Also, most solvent-exposed turns are characterized by flexible motion (model 2, 4, or 5) and have

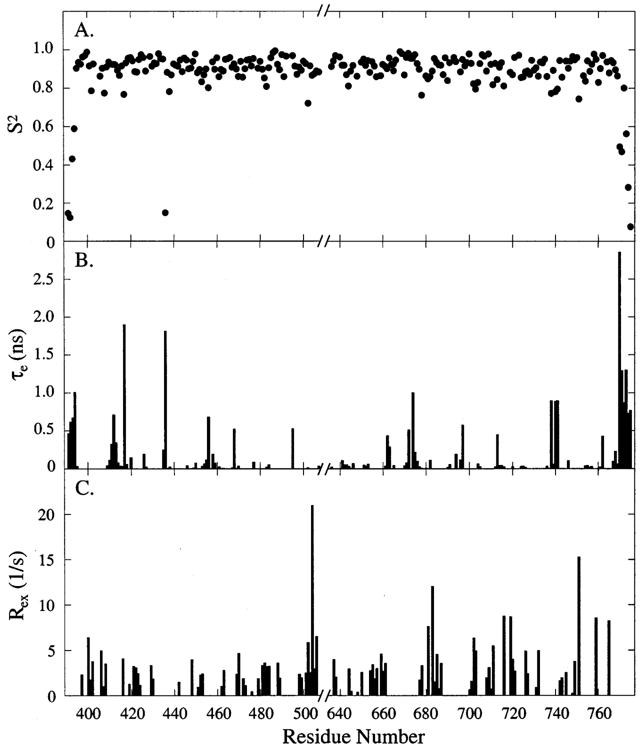

FIGURE 4: Dynamics parameters for S1S2 determined from averages of the parameters at both fields: (A) the generalized order parameter S^2, (B) τ_e, and (C) the chemical exchange term R_{ex} vs residue number.

reduced S^2 values. Using the numbering system corresponding to full-length GluR2 with the signal sequence removed (*48*), residues 406−424 and 451−462 comprise antiparallel β-sheets with a loop between them. In both cases, the β-strands have chemical exchange components (suggesting motion on the microsecond to millisecond time scale), while the loops exhibit motion on multiple time scales. The sequence conservation of the β-sheets but not the loops among non-NMDA subunits could suggest a role for the loop regions in binding to the N-terminal domain, other iGluR subunits, or other iGluR specific binding proteins. The relatively complex motion of the loops also provides an explanation for the inability to assign T457. Other observable motions, which may reflect functional properties, are described below in more detail.

Backbone Dynamics of S1S2

Ligand-Binding Pocket. The ligand-binding pocket can be divided into residues interacting with the α- and γ-constituents of the agonist glutamate. As shown in Figure 5C, residues T480, R485, P478, S654, and E705 interact with the α-constituent of glutamate. Neither T480 nor R485 exhibits exchange, and they are fit to the simplest model of internal motion, model 1. E705, fit to model 2, also does not exhibit exchange. P478 was not characterized due to the lack of an amide proton. While S654 does exhibit exchange, it interacts with both the α-constituent (through the side chain) and the γ-constituent (through the backbone). Since the backbone dynamics of S654 are characterized here, the γ-interaction is more reflective of the measured dynamics. Taken together, the lack of chemical exchange in the α-binding region may suggest a lock-and-key fit, consistent with the well-defined α-substituent binding site observed in the crystal structures (*23*), possibly dictating the conserved structure of the α-substituents of glutamateric agonists. Residues S654, T655, L650, and L703 form the γ-region of the binding pocket, and all exhibit exchange with similar exchange terms. Furthermore, all residues in this region for which α, the parameter characterizing the time scale of exchange, could be calculated exhibit fast exchange (*43*). Such congruent mobility may suggest that the ligand is less tightly bound to this region of the binding site. One possibility is that this motion allows these residues to adapt their conformation to the ligand rigidly bound by the α-substituents. This is evident from the crystal structure in which residues that contact the γ-substituents show some structural rearrangement upon interaction with different ligands (*23*). This "induced fit" mechanism of binding is consistent with the differences between iGluR ligands, which have similar α-substituents but vary in the γ-position. Further implications of agonist interactions with residues in lobe 2 are discussed below.

The Lobe 2 β-Core Is Mobile. An unexpected finding from the dynamics is the presence of chemical exchange in the predominantly β-sheet core of lobe 2. Figure 5D shows the core region colored according to the model. All characterized residues in the lobe 2 β-core from β-8, β-10, and β-11 show exchange, though on different time scales. Motional characterizations of the residues in β-9 are lacking since A646 was not fit to any model and incomplete relaxation data were obtained for Y647. One could postulate that the inability to determine precise relaxation parameters for these residues is due to their significant motional properties. The mobile character of the lobe 2 β-core is unexpected since, based on crystallography, there is no discernible difference between the rmsd of the lobe 2 β-cores of the apo, glutamate-bound, and kainate-bound states and the average *B*-factor of the core of lobe 2 is only ~7.5% greater than that of the lobe 1. When the dynamics are contrasted, the lobe 1 β-core is predominantly fit to model 1 (Figure 5A). On a faster time scale, molecular dynamics simulations indicate that the structural order of lobe 2 is increased upon agonist binding (*49*). Taken together, these results suggest a favored conformation of the lobe 2 core is observed in the crystal structures, but slower time scale motions not observed in the crystal may be present. Interestingly, the artificial linker substituting for the pore-forming region lies between β-8 and β-9. Also, the γ-portion of the binding site is formed by residues in the β-sheet core of lobe 2 on the ends opposite the connection to the pore. Thus, the dynamic properties of the lobe 2 β-core may well have functional consequences.

Hinge Region. Lobes 1 and 2 are connected by two transdomain linkers (Figure 5A,D), which are predominantly β-sheetlike structures. The first is composed of residues 493−500 and contains β-7, while the second is composed of residues 727−734 and contains β-12. Of the residues in the linkers, only those near lobe 2 (L498, G499, L727, and D728) exhibit exchange. These residues lie directly between the amino acids (S497 and I500; L727 and G731) that show changes in backbone dihedral angles between the apo form and the glutamate-bound form of S1S2 in the crystal structure. The motions of these residues suggest a hinge axis very similar to that proposed along helix I from the crystal structure calculations (*23*). Residues in helix I adjacent to the side chain of W767 show exchange, further supporting

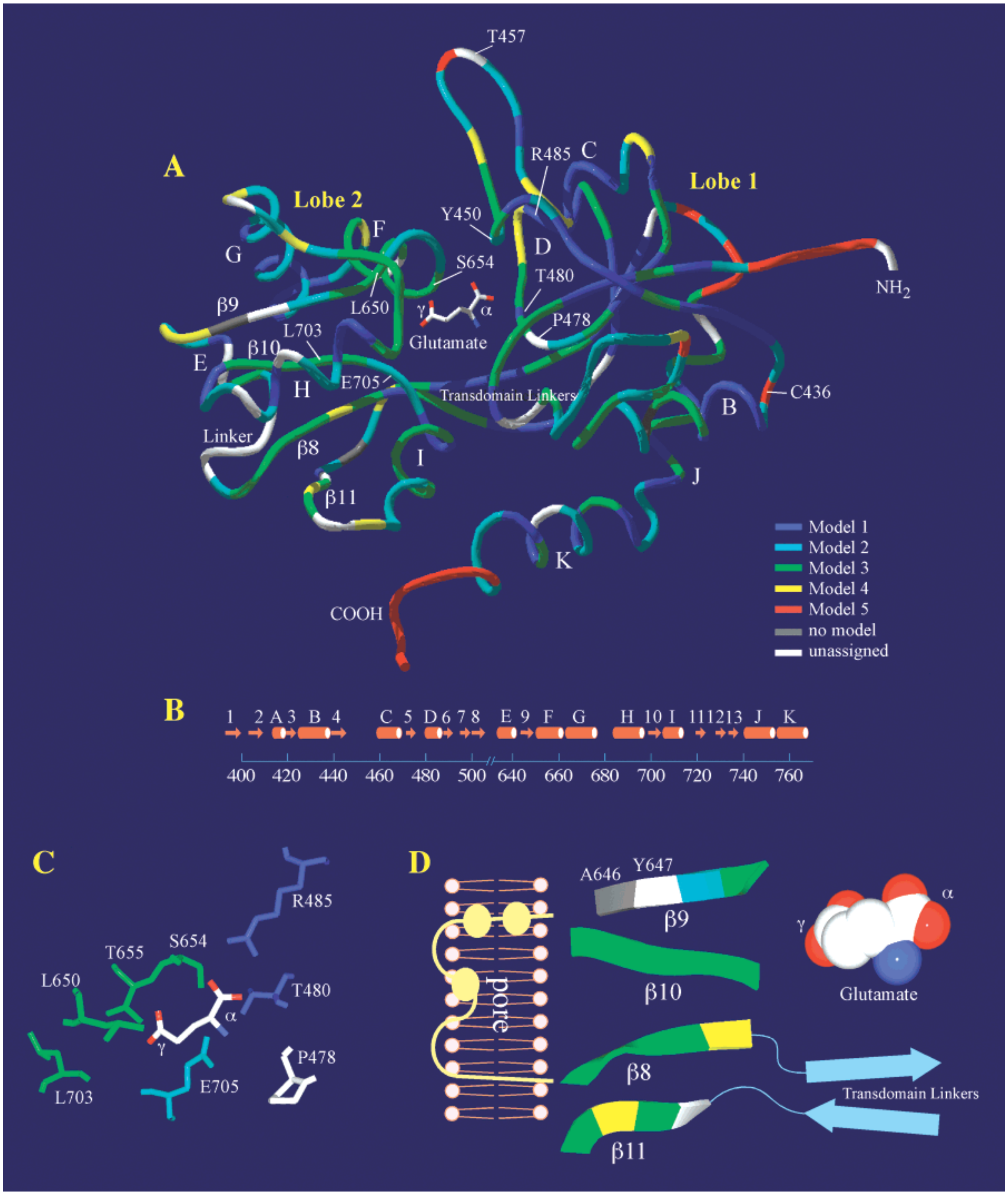

FIGURE 5: (A) S1S2 crystal structure (*23*) with residues colored according to the dynamics model. The models are defined in Table 1. The positions of individual helices are labeled with capital letters according to the scheme in panel B. (B) Representation of the secondary structure following the notation of Armstrong et al. (*22*). (C) Residues forming the α- and γ-portions of the ligand-binding pocket are colored according to the dynamics model. The residues binding the α-constituents of glutamate (R485, T480, P478, and E705) do not exhibit chemical exchange, while those contacting the γ-constituents (S654, T655, L650, and L703) do exhibit chemical exchange. (D) Ribbon diagram of the lobe 2 β-sheet core colored according to the dynamics model. All residues in β-8, β-10, and β-11 exhibit exchange, indicative of conformational exchange. A cartoon of the pore region is shown at the left; the linkers are shown in cyan at the bottom right, and the agonist glutamate is shown at the top right.

this as the axis of rotation. Figure 6A shows an alignment of the residues for which exchange is observed in both transdomain linkers. Interestingly, the side chains of W766 and W767 are directly in line with the residues in the transdomain linkers showing exchange. Falling near the rotational axis, they potentially act as a joint around which the lobes rotate as the linkers kink or bend. Even the most conservative mutation of the tryptophan residues causes drastic destabilization of the molecule, an increased rate of aggregation, and greatly diminished agonist binding affinity (R. L. McFeeters and R. E. Oswald, unpublished results). The importance of these residues and the potential ring stacking of W767 and Y711 suggest that helix K could act as another potential linker anchoring the lobes together. Both transdomain linkers are tied to the relatively mobile β-sheets in the lobe 2 core. Thus, a potential mechanism explaining how domain closure can be propagated to channel opening relates to the mobility of the lobe 2 core. When agonist binds,

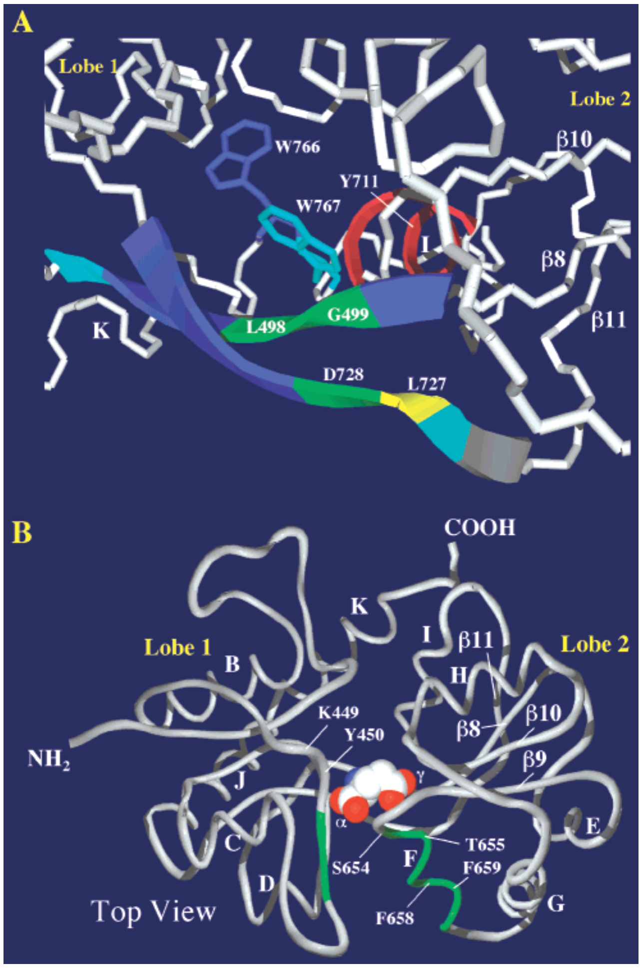

FIGURE 6: (A) Ribbon diagram of the transdomain linkers colored according to dynamics model showing the positions of L498, G499, L727, and D728. Helix I (red) lies near the rotational axis predicted from crystallography. Also shown are the tryptophan side chains (W766 and W767), which potentially form a joint that may cause the twist motion suggested from molecular dynamics simulations (*49*). (B) "Top" view of S1S2 depicting ligand accessibility with the agonist glutamate shown in space filling mode. Residues in helix F and across the binding cleft (fit to model 3, green) exhibit fast chemical exchange. Concerted motion in this region could allow ligand dissociation without reopening of the lobes.

the structure, and possibly the dynamics, of the S497−I500 segment is altered. This linker is directly tied to β-8, which is in turn tied to the pore-forming region. Thus, through β-8, domain closure could be coupled to channel gating. Changes near L727 and D728 could affect β-11, potentially having secondary effects on β-8 and channel function.

Ligand Exit Pathway. The backbone dynamics data provide a plausible exit pathway for ligands that does not require domain opening. Looking down on the binding cleft (Figure 6B), lobe 1 forms one side and lobe 2 the other side of the binding cavity. Residues forming the "top" of the binding site exhibit no microsecond to millisecond motion. Of note, Y450 sterically occludes ligand exit from the top of the binding cavity and seems to lock into place upon agonist binding. Backbone motion may be constrained by the side chain interaction with agonist since continuous residues both N- and C-terminal to K449 and Y450 all exhibit chemical exchange. E705 and part of the transdomain linkers form the "bottom" of the binding site, all of which are fit to model 1. Not all of these residues that form the "back" of the binding cavity exhibit exchange. Those that do exhibit exchange have parameters on different time scales, indicating a lack of cohesive motion. Thus, ligand dissociation without domain reopening would to be limited to the "front" of the binding cavity. Part of the front of the binding cavity is formed by the relatively inflexible α-constituent binding region. However, the remainder is formed by S654, T655, helix F, and residues on the opposite side of the binding cleft. All of these residues exhibit microsecond to millisecond motion with nearly identical fast exchange terms. Coupled with the ring stacking of F658 and F659 in helix F, this suggests concerted motion of the entire helix. This orchestrated movement could provide an exit pathway for ligands, potentially allowing dissociation without domain reopening. Molecular dynamics simulations in which the agonist glutamate was replaced with water in the closed conformation did not show domain reopening throughout the lifetime of the simulation (*49*), suggesting that the lobes could stay in the closed conformation in the absence of ligand. Ligand dissociation without domain reopening could underlie receptor desensitization or inactivation. Comparison to the dynamics of the apo state certainly will shed light on this aspect of binding.

Comparison of Structural Techniques

The major limitation of this work, shared with reports describing the X-ray crystal structures (*22*, *23*) and molecular dynamics simulations (*49*), is that we are studying an excised ligand-binding core rather than an intact receptor. However, the binding curves and IC$_{50}$ values of S1S2 for agonists and antagonists mimic those of the full-length protein (*19*−*21*), so it is likely that the pharmacological properties of the S1S2 construct parallel those of the entire receptor. Thus, these three complementary techniques, which yield consistent results, provide substantial insight into receptor−ligand interactions that is invaluable for drug design. Molecular dynamics calculations suggest lobe 2 is less rigidly ordered than lobe 1, which is confirmed by the backbone dynamics. A mechanism of domain closure with rotation about helix I follows from the crystal structures. The backbone dynamics support this conclusion and suggest L498, G499, L727, and D728 in the transdomain linker actually are perturbed by the closure. Unique to the backbone dynamics measurements, different motions in the ligand-binding site are clearly demarcated and a potential pathway for ligand dissociation without domain reopening is suggested. Taken together, the structure from crystallography, predictions from simulations, and motional characterization from backbone dynamics provide a consistent description of the extracellular iGluR ligand-binding domain, providing some of the mechanistic details of ligand binding and their translation to channel function. On the basis of the available data, a functional model can be proposed: agonist binding results in domain closure, an induced change in the transdomain linker regions, and propagation of binding through the mobile β-8 strand to the pore region, contributing to channel gating. Differential interactions of the γ-constituents of agonists could alter properties of the lobe 2 core, causing differences in channel kinetics, bound time, and binding affinity. Although the flip-flop region is clearly involved in desensitization (*50*), desensitization could be affected by dissociation of the activating agonist through the congruent motion of helix F without reopening of the domains. Intersubunit interactions affecting helix F could contribute to different channel properties based on subunit composition or stoichiometry.

Conclusions

S1S2 is a relatively large protein by current NMR standards (29 kDa). However, TROSY-based relaxation experiments using a fully deuterated protein provide excellent spectra, allowing for a thorough backbone dynamics characterization. The dynamics data provide a number of insights that were not apparent from the crystal structures and molecular dynamics simulations. Residues contacting the agonist exhibit two clearly defined regions, suggesting two different modes of interaction. Those residues of S1S2 contacting the α-substituents exhibit minimal internal motion, whereas residues contacting the γ-substituents exhibit chemical exchange. Different agonists that activate GluR2 have similar α-constituents but varying γ-constituents, suggesting the γ-region of the protein is relatively flexible and binds with an induced fit mechanism, potentially affecting the channel properties of an intact receptor. Chemical exchange in the predominantly β-sheet core of lobe 2 could have functional consequences since two of the β-strands flank the pore-forming transmembrane segments and form part of the γ-region of the binding pocket. In addition, chemical exchange was observed in the transdomain linker regions that form the hinge between lobes 1 and 2, again with potential functional consequences. Chemical exchange with similar kinetics is observed throughout helix F, suggesting concerted motion, which may allow agonist dissociation without complete lobe reopening. Thus, the S1S2 ligand-binding core of GluR2 exhibits internal dynamics on multiple time scales, with regions thought to be important for function undergoing microsecond to millisecond motion. Drug development and the characterization of the mechanism for transducing binding into the opening of the ion channel are dependent upon both the structure of the protein and the details of its dynamic properties, such as those reported here.

ACKNOWLEDGMENT

We thank Dr. Linda Nicholson and especially Norma Pawley for providing the NORMAdyn software package, invaluable discussion, and critical reading of the manuscript. We also thank Dr. Andrew Byrd and Dr. Amanda Altieri for providing the watersled pulse sequence used for diffusional translation, Dr. Eric Gouaux for providing the S1S2 construct, and Dr. Adrienne Loh and Dr. Greg Weiland for helpful discussion and manuscript revision.

SUPPORTING INFORMATION AVAILABLE

Tables of (1) relaxation parameters measured at 500 MHz, (2) relaxation parameters measured at 600 MHz, and (3) dynamics parameters derived from the relaxation measurements. This material is available free of charge via the Internet at http://pubs.acs.org.

REFERENCES

1. Dingledine, R., Borges, K., Bowie, D., and Traynelis, S. F. (1999) *Pharmacol. Rev. 51*, 7−61.
2. Asztely, F., and Gustafsson, B. (1996) *Mol. Neurobiol. 12*, 1−11.
3. Maren, S., and Baudry, M. (1995) *Neurobiol. Learn. Mem. 63*, 1−18.
4. Inagaki, N., Kuromi, H., Gonoi, T., Okamoto, Y., Ishida, H., Seino, Y., Kaneko, T., Iwanaga, T., and Seino, S. (1995) *FASEB J. 9*, 686−691.
5. Weaver, C. D., Yao, T. L., Powers, A. C., and Verdoorn, T. A. (1996) *J. Biol. Chem. 271*, 12977−12984.
6. Chenu, C., Serre, C. M., Raynal, C., Burt-Pichat, B., and Delmas, P. D. (1998) *Bone 22*, 295−299.
7. Patton, A. J., Genever, P. G., Birch, M. A., Suva, L. J., and Skerry, T. M. (1998) *Bone 22*, 645−649.
8. Ault, B., and Hildebrand, L. M. (1993) *J. Pharmacol. Exp. Ther. 265*, 927−932.
9. Carlton, S. M., Hargett, G. L., and Coggeshall, R. E. (1995) *Neurosci. Lett. 197*, 25−38.
10. Gill, S. S., Pulido, O. M., Meuller, R. W., and McGuire, P. F. (1998) *Brain Res. Bull. 46*, 429−434.
11. Nakanishi, N., Schneider, N. A., and Axel, R. (1990) *Neuron 5*, 569−581.
12. O'Hara, P. J., Sheppard, P. O., Thogersen, H., Venezia, D., Haldeman, B. A., McGrane, V., Houamed, K. M., Thomsen, C., Gilbert, T. L., and Mulvhill, E. R. (1993) *Neuron 11*, 41−52.
13. Wo, Z. G., and Oswald, R. E. (1994) *Proc. Natl. Acad. Sci. U.S.A. 91*, 7154−7158.
14. Hollmann, M., Maron, C., and Heinemann, S. (1994) *Neuron 13*, 1331−1343.
15. Bennet, J. A., and Dingledine, R. (1995) *Neuron 14*, 373−384.
16. Wo, Z. G., and Oswald, R. E. (1995) *Trends Neurosci. 18*, 161−168.
17. Wood, M. W., VanDongen, H. M. A., and VanDongen, A. M. J. (1995) *Proc. Natl. Acad. Sci. U.S.A. 92*, 4882−4886.
18. Chen, G. Q., Mayer, M. L., and Gouaux, E. (1999) *Nature 402*, 817−821.
19. Chen, G. Q., and Gouaux, E. (1997) *Proc. Natl. Acad. Sci. U.S.A. 94*, 13431−13436.
20. Kuusinen, A., Arvola, M., and Keinanen, K. (1995) *EMBO J. 14*, 6327−6332.
21. Kuusinen, A., Arvola, M., Oker-Blom, C., and Keinanen, K. (1995) *Eur. J. Biochem. 233*, 720−726.
22. Armstrong, N., Sun, Y., Chen, G. Q., and Gouaux, E. (1998) *Nature 395*, 913−917.
23. Armstrong, N., and Gouaux, E. (2000) *Neuron 28*, 165−181.
24. Mayer, M. L., Olson, R., and Gouaux, E. (2001) *J. Mol. Biol. 331*, 815−836.
25. McFeeters, R. M., Swapna, G. V. T., Montelione, G. T., and Oswald, R. E. (2002) *J. Biomol. NMR 22*, 297−298.
26. Geet, A. L. v. (1970) *Anal. Chem. 42*, 679−680.
27. Raiford, D. S., Fisk, C. L., and Becker, E. D. (1979) *Anal. Chem. 51*, 2050−2051.
28. Zhu, G., Youlin, S., Nicholson, L. K., and Sze, K. H. (1999) *J. Magn. Reson. 143*, 423−426.
29. Delaglio, F., Grzesiek, S., Vuister, G. W., Zhu, G., Pfeifer, J., and Bax, A. (1995) *J. Biomol. NMR 6*, 277−293.
30. Nicholson, L. K., Kay, L. E., Baldisseri, D. M., Arange, J., Young, P. E., Bax, A., and Torchia, D. A. (1992) *Biochemistry 31*, 5253−5263.
31. Altieri, A. S., Hinton, D. P., and Byrd, R. A. (1995) *J. Am. Chem. Soc. 117*, 7566−7567.
32. Barbato, G., Ikura, M., Kay, L. E., Pastor, R. W., and Bax, A. (1992) *Biochemistry 31*, 5269−5278.
33. Pawley, N. H., Wang, C., Koide, S., and Nicholson, L. K. (2001) *J. Biomol. NMR 20*, 149−165.
34. Palmer, A. G., Wright, P. E., and Rance, M. (1991) *Chem. Phys. Lett. 185*, 41−46.
35. Kay, L. E., Torchia, D. A., and Bax, A. (1989) *Biochemistry 28*, 8972−8979.
36. Woessner, D. E. (1962) *J. Chem. Phys. 32*, 647−654.
37. Lipari, G., and Szabo, A. (1982) *J. Am. Chem. Soc. 104*, 4546−4559.
38. Lee, L. K., Rance, M., Chazin, W. J., and Palmer, A. G. (1997) *J. Biomol. NMR 9*, 287−298.
39. Gagne, S. M., Tsuda, S., Spyracopoulos, L., Kay, L. E., and Sykes, B. D. (1998) *J. Mol. Biol. 278*, 667−686.
40. Abragam, A. (1961) *The Principles of Nuclear Magnetism, 1970 Edition*, Clarendon Press, Oxford, U.K.
41. Lee, A. L., and Wand, A. J. (1999) *J. Biomol. NMR 13*, 101−112.

42. Tjandra, N., Wingfield, P., Stahl, S., and Bax, A. (1996) *J. Biomol. NMR 8*, 273−284.
43. Millet, O., Loria, P., Kroenke, C. D., Pons, M., and Palmer, A. G. (2000) *J. Am. Chem. Soc. 122*, 2867−2877.
44. Palmer, A. G., Kroenke, C. D., and Loria, J. P. (2001) *Methods Enzymol. 339*, 204−238.
45. Farrow, N. A., Muhandiram, R., Singer, A. U., Pascal, S. M., Kay, C. M., Gish, G., Shoelson, S. E., Pawson, T., Forman-Kay, J. D., and Kay, L. E. (1994) *Biochemistry 33*, 5984−6003.
46. Mandel, A. M., Akke, M., and Palmer, A. G. (1995) *J. Mol. Biol. 246*, 144−163.
47. Mandel, A. M., and Palmer, A. G. (1996) *Biochemistry 35*, 16009−16023.
48. Hollmann, M., and Heinemann, S. (1994) *Annu. Rev. Neurosci. 17*, 31−108.
49. Arinaminpathy, Y., Sansom, M. S., and Biggin, P. C. (2002) *Biophys. J. 82*, 676−683.
50. Sommer, B., Keinänen, K., Verdoorn, T. A., Wisden, W., Burnashev, N., Herb, A., Köhler, M., Takagi, T., Sakmann, G., and Seeburg, P. H. (1990) *Science 249*, 1580−1584.

BI026010P